AIAA JOURNAL
Vol. 42, No. 6, June 2004

Nonintrusive Pressure and Temperature Measurements in an Underexpanded Sonic Jet Flowfield

M. A. Woodmansee* and V. Iyer*
General Electric Global Research Center, Niskayuna, New York 12309
J. C. Dutton†
University of Illinois at Urbana–Champaign, Urbana, Illinois 61801
and
R. P. Lucht‡
Purdue University, West Lafayette, Indiana 47907

Nonintrusive pressure and temperature measurements are performed in the flowfield of an underexpanded sonic jet using high-resolution nitrogen coherent anti-Stokes Raman scattering (CARS). The jet is operated with a fully expanded jet Mach number of 1.83. The time-averaged CARS measurements start at the jet exit and are spatially well resolved, elucidating the near-field shock structure of the jet. For example, the location of the Mach disk is resolved to within 350 μm. Downstream of the Mach disk, viscous effects cause the slip line between the inner and outer jet regions to transition to an annular shear layer. The measurements also define the curved outer shear layer bounding the jet. The experimental pressure and temperature data are compared to similar quantities extracted from a Reynolds-averaged Navier–Stokes computational-fluid-dynamic (RANS CFD) simulation of the flowfield. Except at the jet exit, the mean CARS measurements and CFD predictions along the centerline and along radial traverses in the jet flowfield are in good agreement. The low-pressure (12 kPa) and low-temperature (98 K) conditions of the Mach 3.3 flow entering the Mach disk, as well as the conditions (107 kPa, 262 K) immediately downstream of the disk, are well resolved. Slight deviations of the experimental mean pressure measurements from the CFD pressure distribution in the outer compressible shear layer suggest the existence of streamwise-oriented vortices. Comparisons between these data and measurements from other streamwise-vortex studies are presented.

Introduction

RECENTLY, interest in the manufacture of supersonic business jets[1] has revitalized the concept of civilian aircraft that cruise at supersonic speeds. Although the ability to travel from New York to Tokyo in less than four hours is tantalizing, a number of technical challenges must be met before this objective can be realized. A sampling of these tasks includes 1) designing aircraft engines that premix, ignite, and burn fuel supersonically, while producing limited nitric oxides, unburned hydrocarbon emissions, and greenhouse gases; 2) maintaining laminar flow over the aircraft wings to reduce aerodynamic drag and increase the maneuverability of the aircraft; and 3) minimizing or diverting the aircraft's sonic wave or boom away from the Earth's surface.

Given the complexity of the problems just listed, a fundamental approach to gain insight into the physics of the flow is quite valuable. Obviously, experimental, numerical, and analytical compressible flow studies of the pressure, temperature, and density fields associated with supersonic aircraft are necessary to address the issues just posed. Moreover, experimental and computational investigators share interest in the thermodynamic-property behavior associated with related devices such as military aircraft engine afterburners, chemical lasers, scramjet combustors, and recoilless rifles. Because of its simplicity, the underexpanded jet is often used as a simplified model of the more complex supersonic flowfields associated with the aforementioned devices. The underexpanded jet flowfield contains viscid and inviscid regions, normal and oblique shocks, and regions of expansion and compression waves. In this study, we use the high-resolution N_2 coherent anti-Stokes Raman-scattering (CARS) technique[2] to acquire nonintrusive measurements of mean pressure and temperature in the flowfield of an underexpanded sonic jet.

Since the late 1940s,[3] the underexpanded jet flowfield has been studied theoretically, numerically, and experimentally. Previous numerical studies often relied on the method of characteristics (MOC) for determining the inviscid velocity field. Owen and Thornhill[3] calculated the Mach number and pressure distributions along the jet centerline of an underexpanded jet up to the Mach disk. Extending the work of Owen and Thornhill,[3] Adamson and Nicholls[4] ascertained the centerline Mach-number distribution and Mach disk location as a function of stagnation pressure [i.e., nozzle pressure ratio (NPR)] over a range of flow conditions in both sonic and supersonic underexpanded jets.

Laser Doppler velocimetry[5] (LDV) has been utilized in a number of studies to gather nonintrusive velocity measurements in underexpanded jet flowfields. Most notably, Eggins and Jackson[6] created a streamwise velocity map of the flowfield of an underexpanded jet. The centerline LDV measurements upstream of the Mach disk agreed well with pitot probe-based velocity measurements. Recently, Rayleigh scattering[7] has proven to be a valuable flow visualization tool for isolating streamwise vortices in the shear layers found in underexpanded sonic and supersonic jet flows.[8–14] First reported by Novopashin and Perepelkin,[14] these stable vortex structures originate from Taylor–Görtler[15] instabilities caused by streamline curvature around the first shock cell in the expanding jet. Similarly, the strength and size of these vortices, which reside at the inside edge of the bounding shear layer, can be amplified by artificial perturbations (e.g., glued sand particles or machined grooves) placed on the inner surface of the nozzle. These perturbations extend through the boundary layer, providing origination sites for the streamwise vortices. Conventional pitot probe measurements through the ring of streamwise vortices around the

Received 28 March 2002; revision received 21 November 2003; accepted for publication 1 December 2003.

*Mechanical Engineer, One Research Circle. Member AIAA.
†Donald Biggar Willett Professor of Engineering, Department of Mechanical and Industrial Engineering, 1206 W. Green Street. Associate Fellow AIAA.
‡Professor, School of Mechanical Engineering. Associate Fellow AIAA.

jet periphery highlight their strength. In one particular case,[11] the pressure variation between two adjacent vortices embodied 61% of the jet's stagnation pressure. It is hypothesized that these counter-rotating vortex structures pump fluid into and out of the jet shear layer.

By implementing a double-pulsed Rayleigh-scattering technique, Fourguette et al.[16] acquired convective velocity measurements of the large-scale structures in the compressible shear layer of a supersonic ($M_j = 1.5$) pressure-matched jet. The authors found that the large-scale structures were highly three dimensional and maintained a convective velocity similar to the large-scale structures present in a two-dimensional compressible mixing layer. Dam et al.[17] collected molecular Rayleigh-scattering images in an underexpanded jet flowfield using a UV excimer laser. Air molecules in the jet flow were used as the scattering medium, for which the intensity of the Rayleigh-scattered light is directly proportional to the local gas density. Unfortunately, in the downstream region of the jet flowfield, Mie scattering from condensed water droplets in the entrained ambient air overwhelmed the molecular scattering signal in most of the images.

Paul et al.[18] and Palmer and Hanson[19] used nitric oxide (NO) and hydroxyl (OH) planar laser-induced fluorescence (PLIF), respectively, to examine the underexpanded jet flowfield. With two counterpropagating 226-nm light sheets to excite transitions within the $A^2\Sigma^+ \leftarrow X^2\Pi$ NO electronic band, Paul et al.[18] utilized the Doppler-shifted fluorescence to deduce the streamwise velocity from a jet operating at a nozzle pressure ratio of NPR $= P_t/P_a = 152$. In a similar fashion, Palmer and Hanson[19] employed a broadband dye laser to excite multiple transitions in the $A^2\Sigma^+ \leftarrow X^2\Pi$ OH manifold near 282 nm in an underexpanded jet operating at NPR $= 60$. By ratioing the fluorescence images from different rotational transitions, Boltzmann-based mean temperature images were acquired. A study of the PLIF experimental uncertainties showed that the error in the inferred temperature in the jet core and downstream of the Mach disk was no more than 10 and 30%, respectively. Recently, Yüceil et al.[20] applied interferometric Rayleigh-scattering and particle-image-velocimetry (PIV) measurement techniques to an underexpanded jet over a range of nozzle pressure ratios. These authors focused primarily on comparing the velocity-measurement techniques, and spatially resolved radial profiles of the streamwise and radial velocity components were presented. These data are insightful in that they highlight subtle features of the jet flowfield, such as the slight curvature of the Mach disk.

High-resolution N_2 CARS[2] is used in the present study to obtain mean pressure and temperature measurements in the flowfield of an underexpanded jet. Gas density is inferred from the ideal-gas equation of state. Interested readers are referred to Ref. 2, which is focused on the CARS technique used here and gives an introduction to high-resolution N_2 CARS spectra. In this paper, mean pressure and temperature (P/T) measurements that were acquired along the centerline and three radial traverses in the underexpanded jet flowfield are presented. The current study focuses on these data to examine the steady fluid-dynamic structures within the flowfield. Many of these features, such as the secondary and tertiary recompression regions and the inner shear layer/slip line, have not been explored in the previous studies just described. To aid in the discussion, the experimental measurements are compared to similar quantities extracted from a two-dimensional Reynolds-averaged Navier–Stokes (RANS) computational-fluid-dynamic (CFD) simulation of the underexpanded jet flowfield. To our knowledge, these measurements represent the first spatially well-resolved, nonintrusive, simultaneous pressure and temperature measurements to date in such a jet flowfield. As a secondary attribute, these measurements provide data for comparison to RANS CFD simulations of similar supersonic jet flowfields.

Experimental Apparatus

CARS System

Figure 1 is a top-view schematic of the CARS system. Starting on the left of the schematic, an injection-seeded Continuum Powerlite Precision 8010 Nd:YAG laser is used to drive the conventional broadband dye laser (BDL) as well as to supply the pump beams for the CARS process. The frequency-doubled Nd:YAG laser emits a coherent, vertically polarized 532-nm laser beam with an energy of approximately 825 mJ/pulse. The repetition rate of the laser is 10 Hz; the temporal width (FWHM) of each pulse is approximately 10 ns. A beam splitter is used to divert 80% of the Nd:YAG energy into the broadband dye laser, leaving the remaining 20% for the formation of the two CARS pump beams. Rhodamine 640 dissolved in methanol is used as the organic dye solution in the BDL. With this solution, the BDL lases at approximately 607 nm and has a linewidth of approximately 130 cm^{-1} FWHM. The conversion efficiency of Nd:YAG energy into BDL energy is approximately 12%.

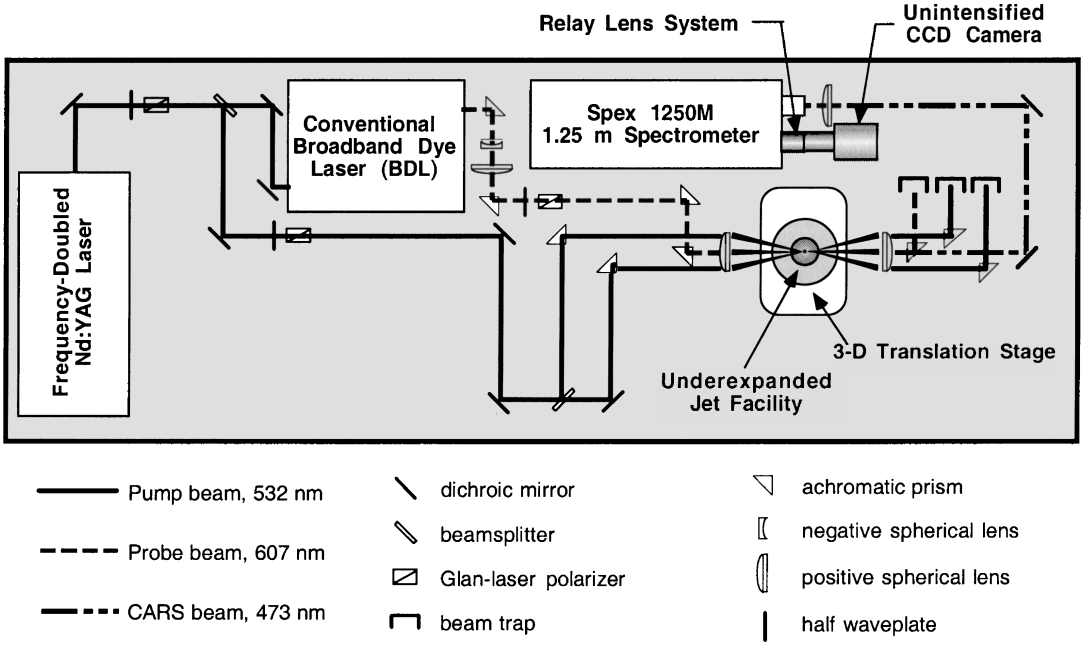

Fig. 1 Top-view schematic of high-resolution N_2 CARS system.

Toward the lower edge of the CARS system sketched in Fig. 1, two pump beams are created by inserting a 50/50 beam splitter into the Nd:YAG beam path. Three right-angle prisms, placed on fine-adjust mounts, are used to direct these two pump beams and the Stokes beam from the BDL onto the focusing lens in a folded BOXCARS[21] phase-matching geometry. An $f = 250$ mm spherical lens focuses the beams to a near diffraction-limited probe volume. Using experimental techniques outlined in Eckbreth,[21] the dimensions of the cylindrical CARS probe volume were determined to be 650 μm in length and 38 μm in diameter, where the spatial boundaries of the probe volume were defined as 10% of the peak signal intensity. In the beam-interaction region, the nonlinear wave mixing process creates a CARS signal at 473 nm. After the CARS signal is generated, the pump, Stokes, and CARS signal beams are recollimated by a second $f = 250$ mm spherical lens. The residual pump and Stokes beams are guided into beam traps. The CARS signal beam is then directed toward a SPEX 1250 1.25-m spectrometer.

At the spectrometer, a positive spherical lens focuses the CARS beam onto the entrance slit. The slit is typically adjusted to an entrance width between 100–130 μm, eliminating most of the directional pump and Stokes laser light not captured by the beam traps. The single-pass Czerny–Turner spectrometer disperses the signal with a 3600-line/mm holographic grating. The frequency-dispersed signal is recollimated and then directed toward the spectrometer exit where it is collected by a relay lens pair coupled to an unintensified charge-coupled device (CCD) camera. The relay lens pair, consisting of two standard Nikon camera lenses with focal lengths of 28 and 210 mm, magnifies the CARS spectrum at the exit of the spectrometer by a factor of 7.5. A 14-bit Photometrics CH250 unintensified CCD camera with a 512×512 pixel array collects the CARS spectra, which are then stored on a Pentium PC. The dispersion of the CARS spectrum on the CCD array is typically 0.0216 cm^{-1}/pixel. Therefore, the entire CARS spectrum (10 cm^{-1} in overall width) occupies approximately 460 of the 512 pixels (90%) on the CCD chip.

Jet Apparatus

The underexpanded jet flowfield is generated using a converging nozzle attached to an air-supply system with $P_t = 960$ kPa capability. The nozzle diameter contracts linearly from the air inlet pipe (19.3 mm i.d.) to the exit orifice (5 mm i.d.); the nozzle inlet and outlet are spaced 102 mm apart. Upstream of the nozzle, the stagnation temperature and pressure are monitored by a hermetically sealed thermistor ($\pm 0.5^\circ$C precision uncertainty) and a 667 kPa full-scale absolute transducer (± 0.5%-of-reading precision uncertainty), respectively. The entire jet flow facility rests on a three-dimensional translation stage. The precision uncertainty of the three orthogonal linear slides that comprise the positioning system is ± 3 μm. A flexible air-supply hose allows the entire flow facility to move freely. Therefore, during data acquisition, the CARS probe volume is maintained at a fixed position while the jet facility is translated. The probe-volume location is referenced spatially to the jet using a technique described in Ref. 22.

Underexpanded Jet Measurements

Flow Conditions and Shadowgraph Visualization

Table 1 outlines the experimental conditions of the underexpanded jet facility studied here. The jet is operated with NPR = 6.17. The jet Reynolds number Re_j, calculated using the velocity, gas viscosity,[23] and thermodynamic conditions of the jet fluid at the nozzle exit, is 1.31×10^5. The convective Mach number[24] for fully expanded conditions, which is a measure of the convective velocity of the large-scale structures within the shear layer with respect to the freestream air, is $M_c = 0.8$. Typically, shear layers with $M_c > 0.3$ are subject to compressibility effects[24] and will grow at a decreased rate when compared to their incompressible counterparts.

Figure 2 contains a shadowgraph photo and measurement-point schematic of the underexpanded jet flowfield operating at the aforementioned conditions. The term *underexpanded* implies that the static pressure of the fluid at the jet exit is greater than the pressure of the ambient fluid. The sonic flow at the exit of the jet is accelerated past Mach 1 by the axisymmetric Prandtl–Meyer expansion fan centered at the lip of the jet nozzle. As evident in Fig. 2a, the oblique interception shock, formed by the reflection of the expansion waves from the jet boundary, terminates at the Mach disk triple point. The barrel-shaped interception shock separates the inner jet core from the outer annulus of jet fluid. These regions are hereafter referred to as the inner and outer jet regions, respectively. The Mach disk is a normal, albeit slightly curved, shock that forces flow along the jet centerline to recompress, nearly matching the downstream conditions of the jet. Downstream from the perimeter of the Mach disk, the inner jet core is separated from the outer jet region by an annular slip line (Fig. 2b). In Fig. 2a, the outer shear layer, which surrounds the inviscid jet core, occludes view of the slip line and the weaker shock cells downstream of the Mach disk. Clearly, as viscous effects become important, these secondary shock structures will weaken as the flow transitions to a fully developed turbulent jet in the far field.

Table 1 Underexpanded jet flowfield parameters

Parameter	Value
Nozzle pressure ratio NPR $= P_t/P_a$	6.17
Jet stagnation pressure P_t, kPa	613
Jet stagnation temperature T_t, K	296
Jet-exit diameter d_j, mm	5.0
Fully expanded jet Mach no. M_j	1.83
Jet Reynolds no. $Re_j \times 10^{-5}$	1.31
Convective Mach no. M_c	0.8
Freestream velocity ratio $r = U_2/U_1$	0
Freestream density ratio $s = \rho_2/\rho_1$	0.6
Mass flow rate $\dot{m}$, g/s	27.8
Mach disk height above exit, mm	7.1

The CARS measurement locations for the centerline and radial traverses are indicated in Fig. 2b. Upstream of the Mach disk, the CARS centerline measurement locations are spaced by $\Delta z = 356$ μm. Downstream of the Mach disk along the centerline and along the seven radial traverses, the spacing between measurement locations is doubled to 712 μm. In this document, only the $z/d_j = 0.0$, 1.28, and 3.0 radial traverses are discussed. Ten time-averaged (100-shot) CARS spectra were collected at each measurement location.

RANS CFD Simulation

The flowfield of the underexpanded jet is simulated using the commercial CFD software Fluent® Version 6.1. A two-equation renormalization group (RNG) k–ε turbulence model is employed to close the two-dimensional axisymmetric RANS governing equations. The inlet conditions are identical to the experimental conditions outlined in Table 1. The time-dependent continuity, momentum, and energy equations are marched to steady state using a coupled implicit scheme with a Newton-type linearization of the flux terms.[25] The code utilizes a finite volume spatial discretization method with a second-order upwind, flux-difference-splitting scheme to evaluate the inviscid (convective) fluxes in the continuity, momentum, and energy equations.[26] The linearized set of coupled equations is solved using a Gauss–Siedel iterative scheme in conjunction with an algebraic multigrid method.[27] The RNG k–ε transport equations are solved separately after the flow equations have been updated at each time step.

The entire computational domain is presented in Fig. 3a. One sidewall of the jet is evident as a discontinuous horizontal white line at the bottom left-hand corner of the image. The jet centerline is collinear with the plot abscissa. The inlet boundary conditions (e.g., stagnation pressure and temperature specified in Table 1) are applied 25 d_j upstream of the nozzle exit. From the nozzle exit, the computational domain extends 20 d_j in both the positive streamwise and radial directions. A constant pressure of 0.98 atm is specified at the open boundaries surrounding the nozzle. A baseline grid of approximately 30,000 quadrilateral cells is used to discretize the two-dimensional axisymmetric domain. However, the grid is refined near the jet exit to capture the near-field jet structures. A region of

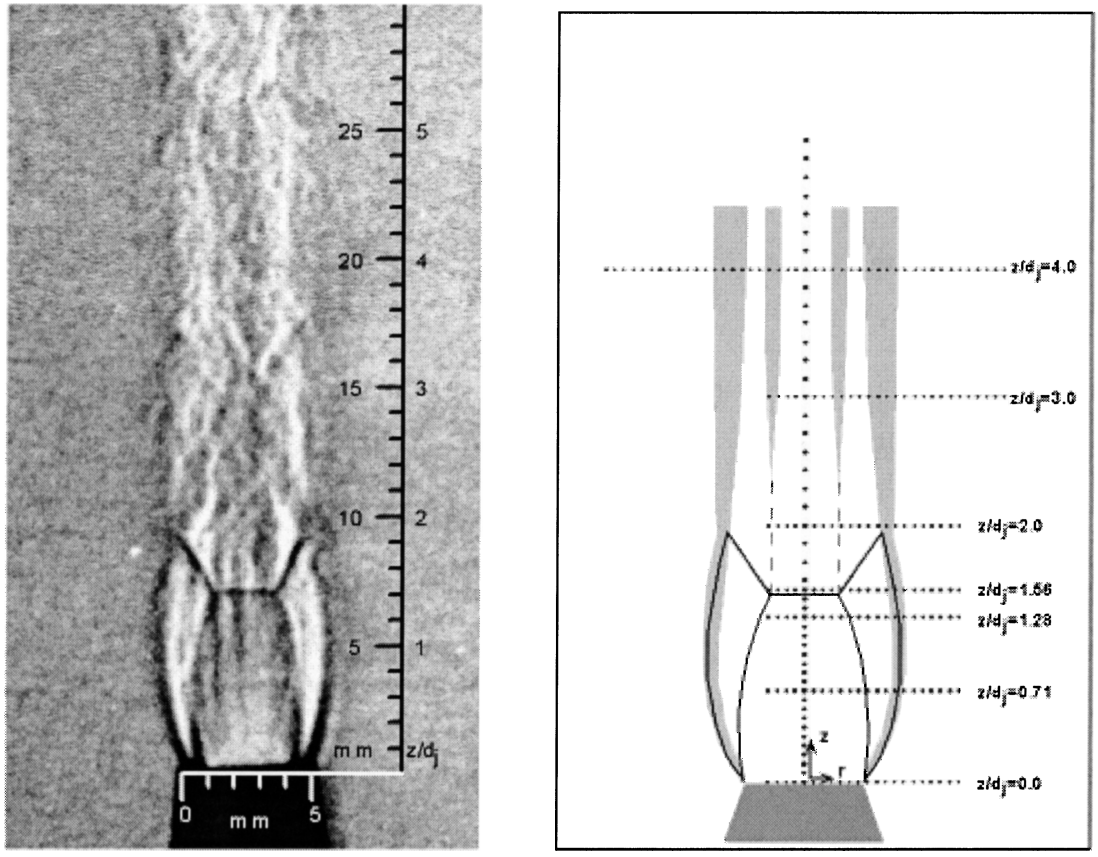

a) b)

Fig. 2 Underexpanded sonic jet (NPR = 6.17): a) shadowgraph and b) CARS measurement-point schematic.

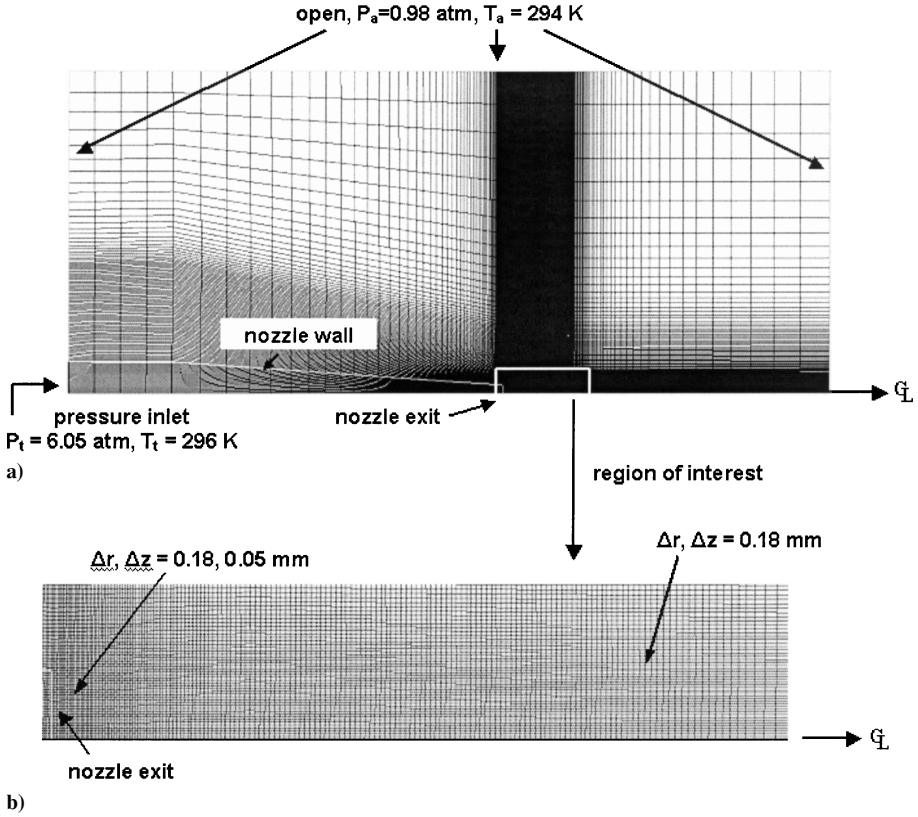

a)

b)

Fig. 3 Underexpanded jet grid: a) entire domain and b) expanded view of nozzle exit.

interest adjacent to the nozzle exit and extending 5 d_j axially and 1 d_j radially is shown as an enlarged image in Fig. 3b. There are approximately 7000 square cells in this refined area with a resolution of 0.035 d_j (0.18 mm). Adjacent to the lip of the nozzle, the axial resolution is increased to 0.01 d_j (0.05 mm) to accurately capture the Prandtl–Meyer fan attached to the lip of the nozzle.

To demonstrate the grid independence of the solution, two refined grids with cell populations of 53,000 and 143,000, respectively, were created. The refinements were achieved by successive quadrupling of the cells in the region of interest shown in Fig. 3b. Figure 4a shows the computed centerline pressure distribution for the coarsest grid and the two refined grids. (The fluid mechanics phenomena associated with the pressure distributions presented in Fig. 4 will be discussed in later sections.) The three distributions are in relatively good agreement, with the Mach disk located at $z/d_j = 1.55$. The flow recompresses to a peak static pressure of 140 kPa downstream of the Mach disk. There is a small discrepancy in the location of the second normal shock (at approximately $z/d_j = 3.15$) between the coarsest grid and the two refined grids. The 30,000-cell solution stations the second Mach disk 0.05 d_j downstream of that for the finer grids. Considering the results in Fig. 4a, the solutions for the two finer grids are essentially indistinguishable. Also of importance, all three solutions show a static pressure of approximately 125 kPa downstream of the second shock. Figure 4b illustrates the radial variation of the static pressure just upstream of the Mach disk at $z/d_j = 1.28$. In this case, all three solutions are in excellent agreement.

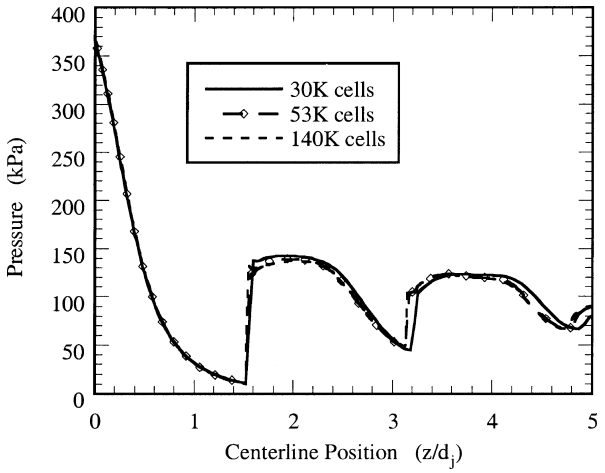

a)

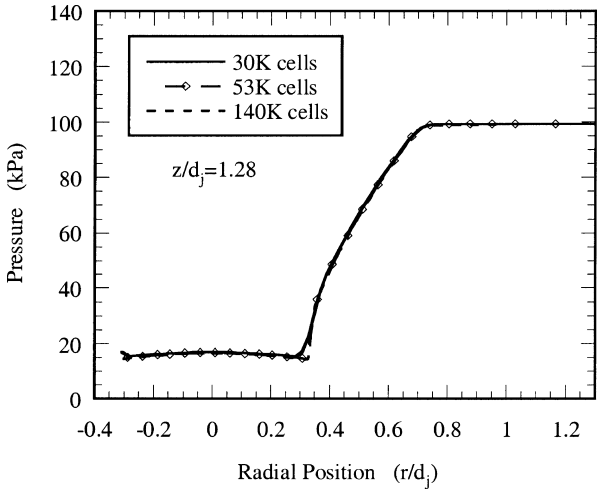

b)

Fig. 4 Numerical grid independence: a) centerline pressure distribution and b) radial pressure distribution at $z/d_j = 1.28$.

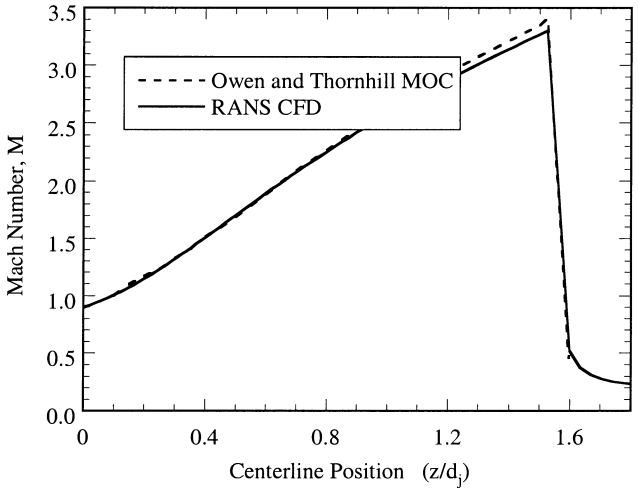

Fig. 5 Centerline Mach-number distribution from Owen and Thornhill[3] MOC analysis and RANS CFD simulation.

Comparing the 140,000-cell solution to an analytical prediction, the centerline Mach-number distribution from the CFD simulation is plotted against the MOC analysis of Owen and Thornhill[3] in Fig. 5. The jet exit resides at $z/d_j = 0.0$, and the flow progresses from left to right in the figure. The two curves are essentially indistinguishable up to $z/d_j = 1.0$.

All computations reported here were performed on a Hewlett–Packard workstation with a single processor. The finest grid computations required five days (80,000 time steps) to converge. The large computational time was attributed to the small time steps (Courant number of 4) used to avoid numerical instabilities. All computational results that are compared to the CARS measurements in subsequent figures are for the finest grid.

Time-Averaged CARS Spectra

Two experimental CARS spectra, acquired upstream and downstream of the Mach disk, are displayed in Fig. 6. The experimental spectra have been least-squares fit by the CARSFIT spectrum-modeling code.[28] The best-fit theoretical spectra are presented as dashed lines in the figure. Because of the low temperature (98 K), low pressure (12 kPa) region upstream of the Mach disk at $z/d_j = 1.42$, only the Q(2)–Q(10) rotational lines in the $v = 0 \rightarrow 1$ vibrational band are populated. (All pressures in this paper are absolute pressures.) The CARSFIT spectrum, created with a Voigt[21] instrument function with 0.10 cm^{-1} FWHM linewidth, closely mimics the experimental spectrum. (In generating the Voigt profile, the ratio of collisional-to-Doppler broadening linewidths[21] was determined to be $\Delta\upsilon_C/\Delta\upsilon_D = 5$; moreover, Doppler-broadening effects were consistently less prominent than collisional-broadening effects throughout the entire flowfield.) Fortunately, the low molecular number density in this region upstream of the Mach disk still contains enough N_2 molecules to generate a viable CARS signal-to-noise ratio[29] (SNR = 187 in Fig. 6a). As a benchmark, the MOC analysis of Owen and Thornhill[3] shown in Fig. 5 suggests that the flow speed is Mach 3.4 before the Mach disk is encountered. The associated static pressure and temperature of 10 kPa and 91 K, determined assuming isentropic flow, compare favorably with the CARS best-fit thermodynamic data of 12 kPa and 98 K, respectively.

An experimental CARS spectrum acquired just downstream of the Mach disk at $z/d_j = 1.49$ is presented in Fig. 6b. At this location, the streamwise-oriented supersonic flow has been recompressed to near-atmospheric conditions. The higher temperature results in population of the outer rotational lines, Q(10)–Q(20), in the CARS spectrum. Indicative of the near ten-fold pressure rise across the shock, the linewidths (FWHM) of the rotational transitions have increased as well. The least-squares theoretical fit of the CARS spectrum, which again agrees favorably with the rotational lines in the experimental spectrum, provides pressure and temperature values of $P = 107$ kPa and $T = 262$ K, respectively.

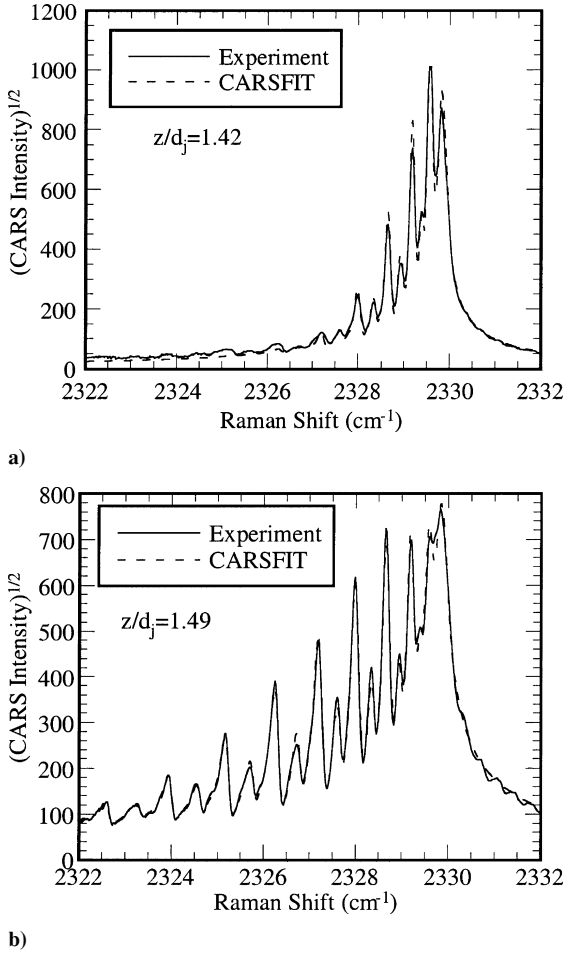

Fig. 6 Experimental spectra acquired a) upstream of the Mach disk at $z/d_j = 1.42$ and b) downstream of the Mach disk at $z/d_j = 1.49$. Best-fit pressures and temperatures are 12 kPa, 98 K and 107 kPa, 262 K, respectively.

Using one-dimensional normal shock relations in conjunction with the isentropic conditions upstream of the Mach disk, the pressure and temperature downstream of this approximately normal shock are estimated to be 133 kPa and 273 K, respectively. Although these values are comparable to the conditions predicted by the CFD simulation just discussed, they are somewhat higher than the CARS measurements. More will be said about this discrepancy in the next section. Finally, considering the disparity in the appearance of the experimental CARS spectra in Figs. 6a and 6b and the small spacing (i.e., 356 μm) between these measurement locations across the Mach disk, it is clear that the experimental pressure and temperature measurements are spatially well resolved. Equally important, the pronounced difference between the shapes of these two spectra clearly illustrates how the Boltzmann population and linewidth of the rotational transitions are strongly tied to the static temperature and pressure, respectively, of the jet fluid.

Centerline Traverse

A comparison between the time-averaged CARS measurements and the associated RANS CFD distributions along the jet centerline is shown in Fig. 7. The pressure and temperature in Figs. 7a and 7b, respectively, are extracted directly from the best-fit CARS spectra. On the other hand, the gas density in Fig. 7c is an inferred quantity obtained from the experimentally measured pressure and temperature values and the ideal-gas equation of state. Although Fig. 7 is similar in some respects to the data presented in Ref. 2, here the CARS data are the mean pressure and temperature determined from 10 time-averaged spectra acquired at each measurement location. The uncertainty bars, barely visible at most streamwise positions, represent one standard deviation of the 10 pressure values. By utilizing time-averaged rather than single-shot spectra, discrepancies caused by random noise sources in the CARS system are minimized, allowing valid comparisons between the experimental and numerical thermodynamic distributions. As an aside, (horizontal) uncertainty bars for the centerline position are unnecessary because the spatial uncertainty of the CARS measurements falls well within the width of the data markers.

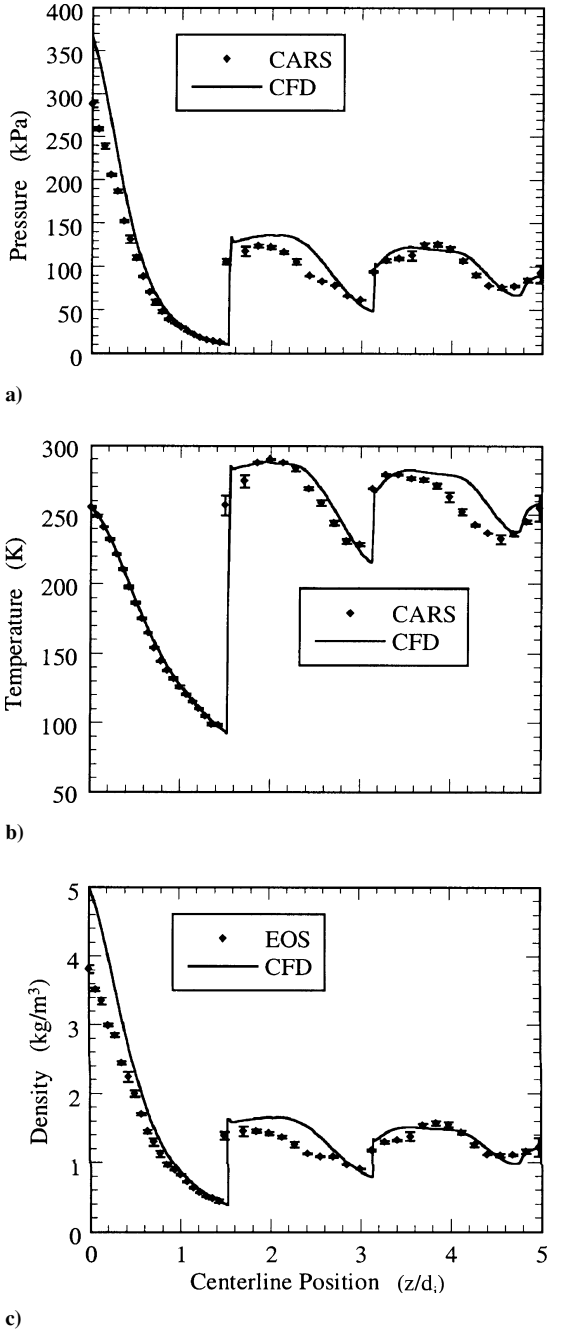

Fig. 7 Time-averaged a) pressure, b) temperature, and c) density measurements along the underexpanded jet centerline.

In Fig. 7a, the largest discrepancy between the high-resolution N_2 CARS pressure measurements and the CFD distribution occurs at the jet exit. Interestingly, the isentropic prediction of exit pressure (324 kPa) essentially bisects the CFD-predicted pressure (360 kPa) and the CARS-measured pressure (288 kPa). One possible explanation for these differences is the extreme sensitivity of the flowfield properties at the jet exit to small changes in the nozzle geometry in the transonic region. Thus, if the nozzle boundary layer in the exit region is not well predicted by the CFD results, significant differences between the CARS measurements and CFD predictions can

be expected. Along these lines, Zapryagaev and Solotchin[12] calculate the displacement thickness of the boundary layer at the nozzle exit using

$$\delta^* = 1.73\{1 + 0.5(\gamma - 1)M^2\}\sqrt{Ld_j/Re_j}$$

where L is the converging or run-up distance of the nozzle. For the particular jet nozzle and associated operating conditions of the current study, the displacement thickness at the orifice is predicted to be $\delta^* = 0.13$ mm. Thus, the boundary-layer displacement thickness occupies over 5% of the jet exit radius, having the potential to induce significant curvature in the sonic line.

However, the most probable reason for the pressure discrepancy at the exit in Fig. 7a is that the CARS spectrum is relatively insensitive to pressure above 200 kPa. In Ref. 2, gas-cell experiments showed that for pressures greater than 100 kPa, the high-resolution N_2 CARS measurements were biased somewhat below the pressure transducer readings with the discrepancy increasing with increasing pressure. Combined with the relatively featureless CARS spectrum for $P > 100$ kPa, the competing collisional narrowing and collisional broadening effects might not be accurately represented in the CARSFIT code.[30] These line-broadening models directly influence the deduced pressure. Another possibility is that at higher molecular number densities, Stark broadening[31] effects from elevated pump laser intensities altered the Q(2)–Q(4) rotational line shapes. In Ref. 32, pressures extracted from CARS spectra collected with pump intensities greater than 350 GW/cm^2 at the probe volume are shown to be greater than those given by a pressure transducer. While this result is opposite to the trend in Fig. 7a, where the CARS pressure is lower than the CFD-predicted pressure, the fact that elevated pump-laser intensities can affect the CARSFIT-deduced pressures and temperatures must be kept in mind. Therefore, great care was taken at the outset of the current experiments to not approach the aforementioned laser intensity threshold.

Acknowledging the discrepancy at the jet exit, the agreement between the CARS and CFD pressure distributions increases as the Mach disk is approached. In this region, Foglesong et al.[33] found the dual-pump CARS technique to be insensitive to the steadily decreasing pressure of the Mach 3.4 flow upstream of the Mach disk. Behind the Mach disk, a small discrepancy in pressure occurs throughout most of the first recompression cell: $1.49 \le z/d_j \le 3.0$ for the current measurements. The flow accelerates once again at the end of this region, reaching Mach 1.3 before encountering a second recompression at $z/d_j \approx 3.0$. Based upon the shallow pressure rise across this region, this second cell might be composed of oblique compression waves rather than a single normal shock.

In Fig. 7b, the agreement between the CARS measurements and CFD simulation of the temperature distribution along the underexpanded jet centerline is very good. Unlike the CARS pressure data, which rely on the linewidth of the individual rovibrational transitions to determine pressure, the temperature is deduced from the relative height of the transitions using Boltzmann statistics. With increasing pressure, the collisional broadening of the transitions raises the background intensity level, introducing uncertainty in the true transition linewidth. However, the relative height of the (shorter) rotational transitions remains nearly constant. Therefore, the better agreement between experimental and numerical data in Fig. 7b is expected.

Upstream of the Mach disk, the CARS temperature measurements closely adhere to the CFD temperature distribution in Fig. 7b. The standard deviation (precision uncertainty) of these average temperature measurements is $\sigma_T = 4$ K. Beginning at $z/d_j = 3.8$, the CARS measurements diverge from the CFD distribution toward lower temperatures. At these downstream locations, the flow along the centerline is rapidly becoming turbulent. Thus, it is possible that the CFD simulation does not accurately model the transition toward a fully developed turbulent jet in the far field.

The experimental pressure and temperature data confirm the presence of two weaker recompression cells downstream of the primary Mach disk. Previous PLIF[18,19] and PIV[20] studies and the shadowgraph image in Fig. 2a exhibit weak evidence of coherent features behind the Mach disk at $z/d_j \approx 3.0$ and 4.5. It is possible that the outer turbulent shear layer diffracts or diffuses the laser sheet (or spatially coherent light column for shadowgraph) downstream of the Mach disk, preventing observation of these weaker recompressions.

Utilizing the CARS pressure and temperature measurements in Figs. 7a and 7b, respectively, and the ideal-gas equation of state, the inferred density distribution along the underexpanded jet centerline is plotted in Fig. 7c. Because the agreement between the CARS and CFD temperature distributions is quite good, the density distribution comparisons are similar to those of pressure. The method for calculating the standard deviation (i.e., precision uncertainty shown as error bars) of the density measurements is given in Ref. 34. Because density is an inferred rather than directly measured quantity, it will not be discussed further. As an aside, it is possible to independently measure gas density[21] of a major species such as N_2 using the integrated intensity of the CARS signal. By ratioing the total CARS beam intensity with a reference intensity acquired at known conditions (e.g., atmospheric), the relative molecular number density, and hence, gas density can be deduced.

Radial Traverses

In Fig. 8, the CARS pressure and temperature measurements acquired in a radial traverse across the jet exit ($z/d_j = 0.0$) are shown. The cylindrical probe volume was oriented such that the major axis (650 μm in length) is oriented circumferentially, maximizing the sensitivity of the CARS technique to the radial gradients within the

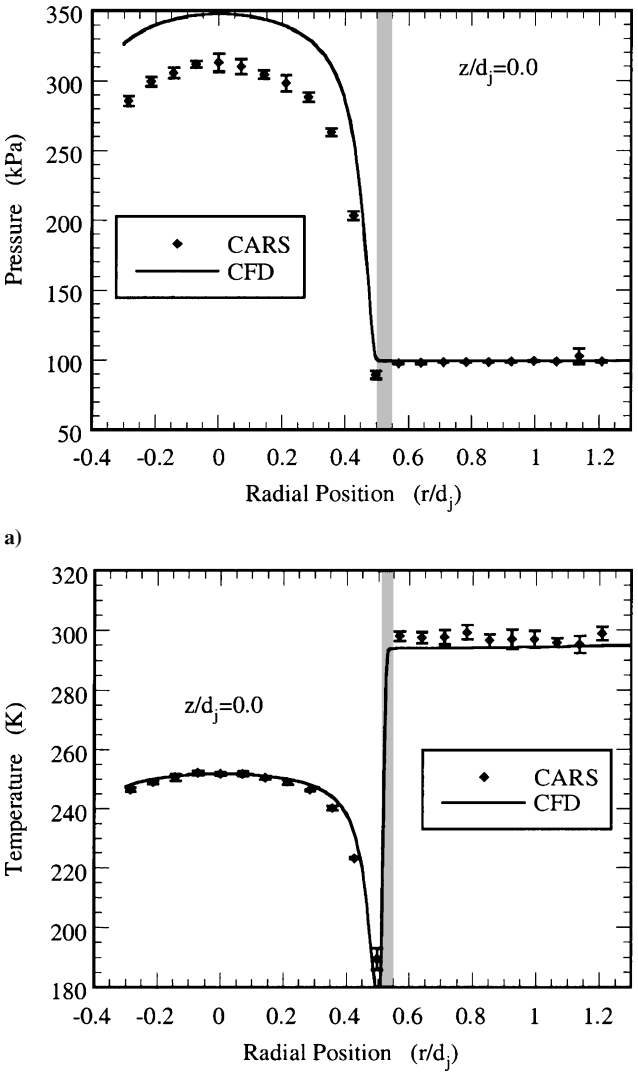

Fig. 8 Distributions across the jet exit at $z/d_j = 0.0$ for a) pressure and b) temperature.

flowfield. Similar to the centerline traverse just discussed, the CFD pressure and temperature distributions are plotted as solid lines. The jet centerline is located at $r/d_j = 0.0$. Note that CARS measurements are acquired past the jet centerline to examine the expected symmetry of the flowfield. In this and following plots, the radial location and width of the compressible shear layer at the outer jet boundary are highlighted using a gray-shaded overlay. The location of this shear layer was defined using the CFD turbulent-kinetic-energy (TKE) distributions, which reach a maximum in the center of the compressible shear layer where the turbulent velocity fluctuations are most intense. The TKE profiles are essentially zero elsewhere. The edges of the shear layer are chosen to be the 10% points on either side of the peak TKE value in the radial profile. The CARS temperature distributions and the shadowgraph image in Fig. 2a corroborate the TKE-based compressible shear-layer location with respect to the jet centerline. For example, at the outer edge of the jet in Fig. 8b, the nearly discontinuous drop in the CARS temperature measurements moving radially inward from the ambient follows the sharp increase in velocity across the compressible shear layer, as would be expected for this adiabatic flowfield.

In Fig. 8a, the CARS pressure measurements within the jet core are qualitatively similar in curvature to the CFD pressure distribution but biased towards lower pressures. The magnitude of this offset at $r/d_j = 0.0$ is slightly less than the centerline pressure measurements in Fig. 7a because the $z/d_j = 0.05$ traverse was extracted from the CFD distribution for Fig. 8a, not the $z/d_j = 0.0$ profile. The lip of the nozzle and associated boundary conditions affected the numerical P/T distributions such that the $z/d_j = 0.05$ traverse was most appropriate for comparison with experimental data. The axisymmetric Prandtl–Meyer expansion fan centered at the nozzle lip dictates the static-pressure distribution across the jet exit. Because of these expansion waves, the jet fluid at the nozzle edge will turn through a larger expansion angle than the flow at the center of the jet, resulting in a higher final velocity. These off-centerline streamlines will therefore include a positive radial velocity (outward) component. However, the constant pressure boundary will reflect these expansion waves as compression waves, forcing the streamlines to curve radially inward as the Mach disk triple point is approached. Compared to its perfectly expanded counterpart, this curvature gives the underexpanded jet its barrellike structure.

As already mentioned, there is sharp temperature gradient across the thin shear layer at $r/d_j = 0.55$ in Fig. 8b. This viscous layer separates the underexpanded jet fluid ($T = 190$ K) from the quiescent air ($T = 297$ K). The experimental and numerical temperature data compare favorably throughout the traverse. Interestingly, the curvature of the pressure distribution across the jet in Fig. 8a is much more pronounced than the curvature of the temperature data in Fig. 8b. A simple regression shows that the radius of curvature of the pressure data in the jet core is the same as for the temperature data raised to the $\gamma/(\gamma - 1)$ power, which is expected for an isentropic flow. Again, this implies that the convex shape of the sonic line at the nozzle exit strongly influences the shape of the associated profiles of the thermodynamic properties. This is to be expected for an inviscid flow. Similarly, one can hypothesize that the data points that do not fall on these arcs yet reside within the extended orifice boundary (i.e., $r/d_j < 0.5$) in Fig. 8 can be influenced by the boundary layer shed from the inner surface of the nozzle. As an aside, a common trend throughout most of the radial traverse figures is that the temperature distribution extracted from the CARS measurements and that of the RANS prediction maintain better agreement than the associated pressure distributions. The most likely reasons for the pressure discrepancy are identical to those just given: 1) the semiempirical linewidth broadening/narrowing model in CARSFIT and 2) possible Stark-broadening effects that appear in regions of the flow with above-ambient N_2 densities.

Upstream of the Mach disk at $z/d_j = 1.28$ (Fig. 9), the compressible shear layer has grown in width and is now located between $0.64 \le r/d_j \le 0.94$. The radial expansion of the jet flow is readily evident in the shift of the midpoint of the shear layer from $r/d_j = 0.55$ at the nozzle exit to $r/d_j = 0.79$ upstream of the Mach disk. As will be seen shortly, the midpoint of the shear layer transitions radially

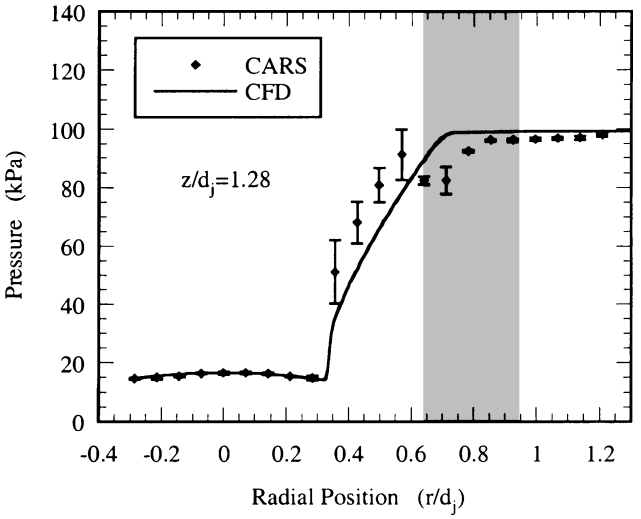

a)

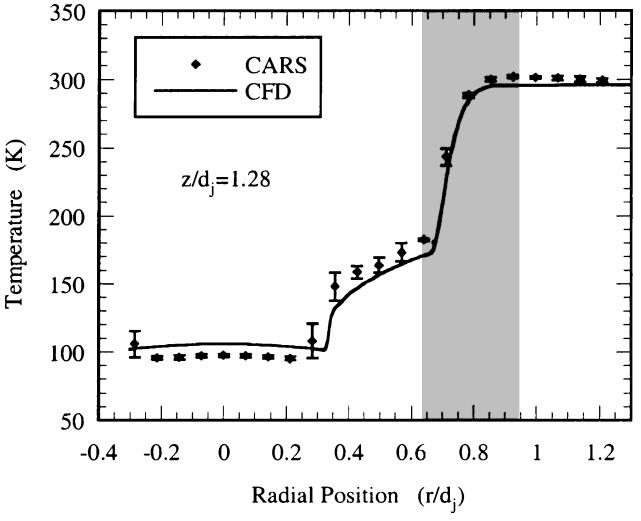

b)

Fig. 9 Distributions upstream of the Mach disk at $z/d_j = 1.28$ for a) pressure and b) temperature.

inward again farther downstream (i.e., the barrel shape of the first shock cell). Moving toward the jet centerline in Fig. 9a, the pressure drops rapidly in the outer jet region between the shear layer and the intercepting shock ($0.36 \le r/d_j < 0.57$). This traverse crosses multiple oblique compression waves emanating from the jet boundary. In this region, the CARS pressure measurements are biased 15 kPa above the CFD distribution. This discrepancy in this barrel-shaped region is most likely caused by a slight difference in the jet's radius of curvature as determined by the CFD simulation. The oblique intercepting shock resides at approximately $r/d_j = 0.35$, causing a near-discontinuous drop in the pressure distribution when moving inward. Compared to the pressure distribution at the nozzle exit, the radial curvature of the pressure distribution in the jet core at $z/d_j = 1.28$ has diminished, leaving an essentially uniform flow of 12 kPa fluid upstream of the Mach disk. In this region, the agreement between the CARS and CFD pressure distributions is very good. However, the CARS temperature measurements in the jet core are biased on average 8 K lower than the CFD temperature distributions in Fig. 9b. Assuming isentropic flow, the experimental data suggest that the inner jet is moving faster (Mach 3.2) than predicted by the CFD simulation (Mach 3.0) at this streamwise location.

In Fig. 9b, the CARS temperature measurements decrease rapidly throughout the jet shear layer moving from the freestream inward. The CARS measurements follow the rapid decrease in temperature from 300 to 182 K at the edge of the outer jet region. Here, Mie

scattering from condensed moisture was visible to the unaided eye as the laser beams irradiated the convecting ice particles. Assuming that the ambient air diffuses to the inner edge of the shear layer, the ice particulate (employed in studies already mentioned[8–11,35] for flow-visualization purposes) resides in a fairly narrow annulus of the jet flowfield, $0.64 \leq r/d_j < 0.77$. Between $0.36 \leq r/d_j < 0.57$, the CARS temperature measurements are biased 11 K above the CFD distribution. Invoking the isentropic flow assumption just mentioned, the magnitude of the bias is consistent with the pressure measurements in the same region shown in Fig. 9a. Notwithstanding the differences in the outer jet region, the agreement between the CARS temperature measurements and the CFD temperature distribution in Fig. 9b is quite good. Similarly, the spatial resolution of the CARS measurements is refined enough to pick up the temperature gradient at the inner edge of the shear layer, where $\Delta r = 1$ mm.

Although not shown here for reasons of brevity, a radial traverse at $z/d_j = 1.56$, immediately downstream of the Mach disk, was also acquired. The slip line downstream of the Mach disk generates a nearly discontinuous junction in the temperature profile between the inner and outer jet regions at this location. This boundary between the warm, subsonic fluid downstream of the normal shock and the surrounding cold, supersonic outer jet region is less than 700 μm in thickness. As one would expect from the disparate velocities in these regions, this slip line transitions to an inner shear layer farther downstream.

At the $z/d_j = 3.0$ radial traverse in Fig. 10, gray-shaded overlays are used to denote the inner and outer shear layers. The inner shear layer is quite thin at this location, extending between $0.19 \leq r/d_j \leq 0.29$. Also, the outer shear-layer region now resides between $0.52 \leq r/d_j \leq 1.02$. Clearly, at these downstream locations, this growing outer shear layer, separating the jet fluid from the ambient air, has engulfed a larger portion of the outer jet flow. At this particular location, the once inviscid near field is transitioning to a constant-pressure turbulent jet. The inner jet shear layer mixes the warm ($T = 220$ K) jet core fluid with the colder ($T = 170$ K) outer jet region. Referring back to Fig. 7, the $z/d_j = 3.0$ radial traverse is acquired just upstream of a second, weaker recompression region. Based on the CFD Mach-number distribution, the flow in this second shock cell reaccelerates to approximately Mach 1.3 such that the pressure and temperature of the fluid in the jet core region at $z/d_j = 3.0$ drop to subatmospheric conditions. Interestingly, the agreement between the CARS pressure data and the CFD distribution in Fig. 10a is generally quite good, as is also the case for the temperature data in Fig. 10b.

One clear discrepancy between the CARS measurements and the CFD simulation is the presence of a local pressure minimum at the inner edge of the outer shear layer. In Fig. 10a, the experimental pressure measurements diverge from the numerical simulation between $0.57 \leq r/d_j \leq 0.85$, reaching a local minimum at $r/d_j = 0.711$. Similar depressions are also evident in the shear layer at $z/d_j = 0.71$, 1.28 (Fig. 9a), 1.56, 2.0, and 4.0 (see Ref. 22 for plots of these data). We hypothesize that in this region the low static pressure reflects the presence of a streamwise-oriented vortex. As mentioned in the Introduction, past studies[8–13] have shown that strong, stable vortices can attach to the inner surface of the nozzle and form streamwise-oriented counter-rotating vortex pairs around the periphery of the jet. Arnette et al.[11] demonstrated that streamline curvature is necessary to initiate the Taylor–Görtler instabilities that lead to these streamwise-oriented vortices. Similarly, other investigators have added artificial roughness elements to the nozzle lip to increase the vortices' strength. To quantify whether the current nozzle embodies artificial[12] ($R_a = 50^+$ μm) or natural[12] ($R_a \approx 2$ μm) roughness elements (the latter solely attributed to the machining process), surface profilometry measurements were acquired prior to the CARS experiments using a Taylor–Hobson Surtronic 3^+ profilometer. The multiple longitudinal and circumferential scans made on the inner surface of the nozzle provided an arithmetic mean roughness of $R_a = 2.5$ μm, denoting natural surface roughness. Compared to the boundary-layer displacement thickness ($\delta^* \approx 0.13$ mm), $R_a/\delta^* = 0.02$, and so one would conclude that these small roughness elements should cause relatively weak vortex structures.

Figure 11 is a plot of the outer shear-layer boundary as a function of r/d_j and z/d_j (flow vertically upward); note the difference in ordinate and abscissa scales. The locations of the local pressure minima as determined by the CARS measurements within the outer shear layer are also plotted as black diamonds. The experimental pressure minima approximately track the curved inner edge of the

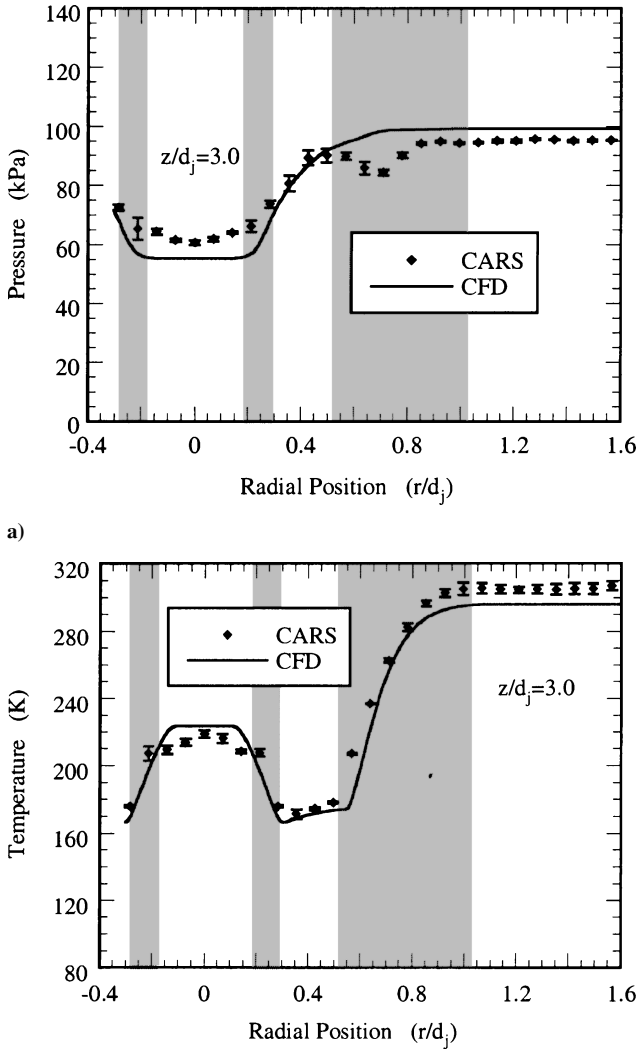

Fig. 10 Distributions at $z/d_j = 3.0$ for a) pressure and b) temperature.

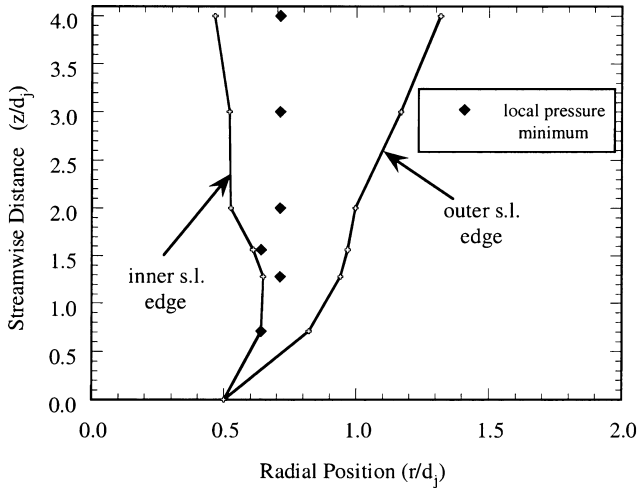

Fig. 11 Radial location of local pressure minimum within outer shear layer.

shear layer, which is consistent with the results of Arnette et al.[11] Not surprisingly, the magnitude of the local pressure depressions ($P = 86 \pm 3$ kPa) is comparable to those found in the "clean" nozzle configuration of Krothapalli et al.[10] Similarly, the strength of these depressions does not change significantly with streamwise distance; this result is also in agreement with the conclusions of Ref. 10. Admittedly, these relatively weak vortices differ greatly from their artificially instigated[13] counterparts, where peak-to-peak pressure variations between neighboring vortex cores exceeded 100 kPa. Although only one circumferential position about the nozzle periphery was characterized in this study, a future application of this CARS technique would be to map the circumferential pressure distribution at different radii and streamwise stations. Because high-resolution N_2 CARS is a nonintrusive technique, these data would alleviate concerns introduced by pitot probe interference. Finally, it is clear that the two-dimensional CFD simulation cannot model a three-dimensional flow structure such as a streamwise vortex. The fact that the CARS measurements consistently diverge from the CFD pressure distribution in the outer shear layer supports the hypothesis that a three-dimensional structure, such as a streamwise vortex, exists at this location.

Summary

Nonintrusive, spatially well-resolved measurements of pressure and temperature were acquired in the flowfield of an underexpanded sonic jet operating at NPR = 6.17. Using the ideal-gas equation of state, gas density was also observed. Centerline and radial traverses were captured throughout the jet flowfield. These results are compared to a Reynolds-averaged Navier–Stokes computational-fluid-dynamics (CFD) simulation of the underexpanded jet. Care was taken to examine the grid independence, numerical accuracy, and convergence criteria of the numerical simulation.

With the high spatial resolution of these measurements, the pronounced differences in pressure and temperature of the flow just upstream (12 kPa, 98 K) and downstream (107 kPa, 262 K) of the Mach disk are easily quantified. The coherent anti-Stokes Raman scattering (CARS) pressure measurements consistently fall below the CFD pressure distribution at the jet exit. This discrepancy is attributed to the decreased pressure sensitivity of the CARS technique at above-ambient pressures, where competing collisional narrowing and collisional broadening effects alter the shape of the $v = 0 \rightarrow 1$ N_2 CARS spectrum. Similarly, weakly coupled Stark-broadening effects at these gas densities might have altered the shape of the N_2 bandhead. However, the agreement between the experimental and numerical data increases as the Mach disk is approached. Further, the experimental measurements along the centerline locate a number of weaker flow-recompression regions downstream of the Mach disk. The CARS temperature data are in very good agreement with the computational results through the Mach disk but begin to diverge from the CFD distribution as the jet transitions to a turbulent flowfield.

Overall, the agreement between the CARS measurements and the CFD distributions along the three radial traverses presented here is good. The spatially well-resolved measurements highlight a number of interesting thermodynamic property trends in the outer compressible shear layer. First, the CARS temperature measurements faithfully follow changes in velocity as one would expect for a perfect gas where temperature and velocity are related adiabatically via the Mach number and stagnation conditions. Thus, the radial location of the outer shear layer was corroborated by both the experimental temperature measurements and CFD turbulent-kinetic-energy profiles. Second, these measurements show that the slip line, which emanates from the Mach disk triple point and separates the inner jet core from the outer jet region, evolve into an inner shear layer with increasing downstream distance. Past studies have failed to describe the evolution of the slip line into an inner shear layer. Although this free shear layer is rather weak (i.e., the two freestreams embody a small velocity difference), it can influence the transition point of the underexpanded jet into a fully developed turbulent stream in the far field. Clearly, with the presence of two concentric shear layers the inviscid jet core will decay into a turbulent stream at an accelerated rate as compared to a perfectly expanded jet with a single shear layer.

Finally, the CARS pressure measurements consistently form local minima at the inner edge of the outer shear layer. This phenomenon is thought to be caused by weak streamwise vortices that are attached to the inner surface of the nozzle. The locations of these pressure depressions track the curved inner boundary of the outer shear layer, providing evidence of Taylor–Görtler instabilities that lead to the streamwise vortices. The magnitude of the pressure divergence from atmospheric conditions at these locations is consistent with other underexpanded jet studies that employ smooth converging nozzles with natural roughness elements.

Acknowledgments

Funding for this research was provided through the Army Research Office (Grant DAAD19-01-1-0367) with Thomas L. Doligalski as Technical Monitor. The authors thank Xuelei Zhu of Fluent, Inc., and Rajeev Jaiman of the University of Illinois at Urbana–Champaign for their assistance with the underexpanded jet simulation. Joel Kuehner, also of the University of Illinois, provided insight into spectral phenomena evident in the experimental coherent anti-Stokes Raman-scattering data. Finally, Clark Mikkelsen and Kevin Kennedy of the U.S. Army Aviation and Missile Command assisted with some initial computations of the jet flowfield.

References

[1]Mack, R. J., "An Analysis of Measured Sonic-Boom Pressure Signatures from a Langley Wind-Tunnel Model of a Supersonic Cruise Business Jet Concept," NASA Tech Briefs Rept. LAR-16277, Feb. 2001.

[2]Woodmansee, M. A., Lucht, R. P., and Dutton, J. C., "Development of High-Resolution N_2 Coherent Anti-Stokes Raman Scattering for Measuring Pressure, Temperature, and Density in High-Speed Gas Flows," *Applied Optics*, Vol. 39, No. 33, 2000, pp. 6243–6256.

[3]Owen, P. L., and Thornhill, C. K., "The Flow in an Axially-Symmetric Supersonic Jet from a Nearly-Sonic Orifice into a Vacuum," Aeronautical Research Council, Rept. 2616, Crown Publishing, Sept. 1948.

[4]Adamson, T. C., Jr., and Nicholls, J. A., "On the Structure of Jets from Highly Underexpanded Nozzles into Still Air," *Journal of the Aerospace Sciences*, Vol. 26, No. 1, 1959, pp. 16–24.

[5]Adrian, R. J., "Laser Velocimetry," *Fluid Mechanics Measurements*, edited by R. J. Goldstein, Taylor and Francis, Washington, DC, 1996, pp. 175–293.

[6]Eggins, P. L., and Jackson, D. A., "Laser-Doppler Velocity Measurements in an Under-Expanded Free Jet," *Journal of Physics D: Applied Physics*, Vol. 7, 1974, pp. 1894–1906.

[7]Smits, A. J., and Dussauge, J.-P., *Turbulent Shear Layers in Supersonic Flow*, AIP Press, Woodbury, NY, 1996, pp. 39–41.

[8]Kim, J.-H., and Samimy, M., "On Mixing Enhancement via Nozzle Trailing-Edge Modifications in High-Speed Jets," *AIAA Journal*, Vol. 38, No. 5, 2000, pp. 935–937.

[9]Krothapalli, A., Buzyna, G., and Lourenco, L., "Streamwise Vortices in an Underexpanded Axisymmetric Jet," *Physics of Fluids A*, Vol. 3, No. 8, 1991, pp. 1848–1851.

[10]Krothapalli, A., Strykowski, P. J., and King, C. J., "Origin of Streamwise Vortices in Supersonic Jets," *AIAA Journal*, Vol. 36, No. 5, 1998, pp. 869–872.

[11]Arnette, S. A., Samimy, M., and Elliott, G. S., "On Streamwise Vortices in High Reynolds Number Supersonic Axisymmetric Jets," *Physics of Fluids A*, Vol. 5, No. 1, 1993, pp. 187–202.

[12]Zapryagaev, V. I., and Solotchin, A. V., "An Experimental Investigation of the Nozzle Roughness Effect on Streamwise Vortices in a Supersonic Jet," *Journal of Applied Mechanics and Technical Physics*, Vol. 38, No. 1, 1997, pp. 78–86.

[13]Zapryagaev, V. I., and Solotchin, A. V., "Development of Streamwise Vortices in the Initial Section of a Supersonic Non-Isobaric Jet in the Presence of Microroughness of the Inner Nozzle Surface," *Fluid Dynamics*, Vol. 32, No. 3, 1997, pp. 465–469.

[14]Novopashin, S. A., and Perepelkin, A. L., "Axial Symmetry Loss of a Supersonic Preturbulent Jet," *Physics Letters A*, Vol. 135, No. 4–5, 1989, pp. 290–293.

[15]Schlichting, H., and Gersten, K., *Boundary Layer Theory*, Springer-Verlag, Berlin, 2000, p. 26.

[16]Fourguette, D. C., Mungal, M. G., and Dibble, R. W., "Time Evolution of the Shear Layer of a Supersonic Axisymmetric Jet," *AIAA Journal*, Vol. 29, No. 7, 1991, pp. 1123–1130.

[17]Dam, N. J., Rodenburg, M., Tolboom, R. A. L., Stoffels, G. G. M., Huisman-Kleinherenbrink, P. M., and ter Meulen, J. J., "Imaging of an Underexpanded Nozzle Flow by UV Laser Rayleigh Scattering," *Experiments in Fluids*, Vol. 24, 1998, pp. 93–101.

[18]Paul, P. H., Lee, M. P., and Hanson, R. K., "Molecular Velocity Imaging of Supersonic Flows Using Pulsed Planar Laser-Induced Fluorescence of NO," *Optics Letters*, Vol. 14, No. 9, 1989, pp. 417–419.

[19]Palmer, J. L., and Hanson, R. K., "Temperature Imaging in a Supersonic Free Jet of Combustion Gases with Two-Line OH Fluorescence," *Applied Optics*, Vol. 35, No. 3, 1996, pp. 485–499.

[20]Yüceil, K. B., Ötügen, M. V., and Arik, E., "Interferometric Rayleigh Scattering and PIV Measurements in the Near Field of Underexpanded Sonic Jets," AIAA Paper 2003-0917, Jan. 2003.

[21]Eckbreth, A. C., *Laser Diagnostics for Combustion Temperature and Species*, Gordon and Breach, Amsterdam, 1996.

[22]Woodmansee, M. A., "Experimental Measurements of Pressure, Temperature, and Density Using High-Resolution N_2 Coherent Anti-Stokes Raman Scattering," Ph.D. Dissertation, Dept. of Mechanical and Industrial Engineering, Univ. of Illinois, Urbana, IL, Aug. 1999.

[23]White, F. M., *Viscous Fluid Flow*, McGraw–Hill, New York, 1991, pp. 28, 29.

[24]Dutton, J. C., "Compressible Turbulent Free Shear Layers," AGARD/VKI Special Course, *Turbulence in Compressible Flows*, AGARD-R-819, 1997, pp. 2-1–2-42.

[25]Weiss, J. M., Maruszewski, J. P., and Smith, W. A., "Implicit Solution of Preconditioned Navier–Stokes Equations Using Algebraic Multigrid," *AIAA Journal*, Vol. 37, No. 1, 1999, pp. 29–36.

[26]Roe, P. L., "Characteristic Based Schemes for the Euler Equations," *Annual Review of Fluid Mechanics*, Vol. 18, 1986, pp. 337–365.

[27]Hutchinson, B. R., and Raithby, G. D., "A Multigrid Method Based on the Additive Correction Strategy," *Numerical Heat Transfer*, Vol. 9, 1986, pp. 511–537.

[28]Palmer, R. E., "The CARSFT Computer Code for Calculating Coherent Anti-Stokes Raman Spectra: User and Programmer Information," Sandia, Rept. SAND89-8206, Albuquerque, NM, Feb. 1989.

[29]Goss, L. P., "CARS Instrumentation for Combustion Applications," *Instrumentation for Flows with Combustion*, edited by A. M. K. P. Taylor, Academic Press, London, 1983, pp. 251–322.

[30]Koszykowski, M. L., Farrow, R. L., and Palmer, R. E., "Calculation of Collisionally Narrowed Coherent Anti-Stokes Raman Spectroscopy Spectra," *Optics Letters*, Vol. 10, No. 10, 1985, pp. 478–480.

[31]Woodmansee, M. A., Lucht, R. P., and Dutton, J. C., "Stark Broadening and Stimulated Raman Pumping in High-Resolution N_2 Coherent Anti-Stokes Raman Scattering Spectra," *AIAA Journal*, Vol. 40, No. 6, 2002, pp. 1078–1087.

[32]Woodmansee, M. A., Lucht, R. P., and Dutton, J. C., "Laser Induced Perturbation Effects in High-Resolution N_2 CARS Spectra," AIAA Paper 2001-0418, Jan. 2001.

[33]Foglesong, R. E., Green, S. M., Lucht, R. P., and Dutton, J. C., "Dual-Pump Coherent Anti-Stokes Raman Scattering for Simultaneous Pressure/Temperature Measurement," *AIAA Journal*, Vol. 36, No. 2, 1998, pp. 234–240.

[34]Kline, S. J., and McClintock, F. A., "Describing Uncertainties in Single-Sample Experiments," *Mechanical Engineering*, Vol. 75, No. 1, 1953, pp. 3–8.

[35]King, C. J., Krothapalli, A., and Strykowski, P. J., "Streamwise Vorticity Generation in Supersonic Jets with Minimal Thrust Loss," AIAA Paper 94-0661, Jan. 1994.

J. P. Gore
Associate Editor